Solid Earth

Porosity and permeability determination of organic-rich Posidonia shales based on 3-D analyses by FIB-SEM microscopy

Georg H. Grathoff[1]**, Markus Peltz**[1]**, Frieder Enzmann**[2]**, and Stephan Kaufhold**[3]

[1]Department of Geography and Geology, EMA University of Greifswald, Greifswald, 17489, Germany
[2]Institute for Geosciences, J. Gutenberg University Mainz, Mainz, 55128, Germany
[3]Bundesanstalt für Geowissenschaften und Rohstoffe, Hannover, 30655, Germany

Correspondence to: Georg H. Grathoff (grathoff@uni-greifswald.de)

Abstract. The goal of this study is to better understand the porosity and permeability in shales to improve modelling fluid and gas flow related to shale diagenesis. Two samples (WIC and HAD) were investigated, both mid-Jurassic organic-rich Posidonia shales from Hils area, central Germany of different maturity (WIC R_0 0.53 % and HAD R_0 1.45 %). The method for image collection was focused ion beam (FIB) microscopy coupled with scanning electron microscopy (SEM). For image and data analysis Avizo and GeoDict was used. Porosity was calculated from segmented 3-D FIB based images and permeability was simulated by a Navier Stokes–Brinkman solver in the segmented images.

Results show that the quantity and distribution of pore clusters and pores (≥ 40 nm) are similar. The largest pores are located within carbonates and clay minerals, whereas the smallest pores are within the matured organic matter. Orientation of the pores calculated as pore paths showed minor directional differences between the samples. Both samples have no continuous connectivity of pore clusters along the axes in the x, y, and z direction on the scale of 10 to 20 of micrometer, but do show connectivity on the micrometer scale. The volume of organic matter in the studied volume is representative of the total organic carbon (TOC) in the samples. Organic matter does show axis connectivity in the x, y, and z directions. With increasing maturity the porosity in organic matter increases from close to 0 to more than 5 %. These pores are small and in the large organic particles have little connection to the mineral matrix. Continuous pore size distributions are compared with mercury intrusion porosimetry (MIP) data. Differences between both methods are caused by resolution limits of the FIB-SEM and by the development of small pores during the maturation of the organic matter. Calculations show no permeability when only considering visible pores due to the lack of axis connectivity. Adding the organic matter with a background permeability of 1×10^{-21} m^2 to the calculations, the total permeability increased by up to 1 order of magnitude for the low mature and decreases slightly for the overmature sample from the gas window. Anisotropy of permeability was observed. Permeability coefficients increase by 1 order of magnitude if simulations are performed parallel to the bedding. Our results compare well with experimental data from the literature suggesting that upscaling may be possible in the future as soon as maturity dependent organic matter permeability coefficients can be determined.

1 Introduction

The investigated organic-rich Posidonia shales are mid-Jurassic in age from the Hils Syncline of northwestern Germany. The investigated samples come from a larger sample set studied at the BGR as part of their NIKO project (Kaufhold et al., 2016). Kaufhold et al. (2016) compared the direct porosity measurements of focused ion beam – scanning electron microscopy (FIB-SEM) and micro computer tomography (μCT) with the indirect methods of mercury intrusion porosimetry (MIP) and gas adsorption (N$_2$ and CO$_2$) and found that 80 % of the porosity were pores with radii below 30 nm, which can be barely detected by FIB-SEM and was not recognizable by μCT. For our study we took a more detailed look at two of the samples: (1) Wickensen (WIC) with the lowest vitrinite reflectance (R_0) of 0.53 % represent-

Table 1. Compilation of porosity, permeability and TOC data from recent Posidonia shale studies. * Since the bedding plane was tilted, calculations were not performed strictly parallel or perpendicular to the bedding plane. ** TOC contents in wt % were estimated by assuming a density of $1.25\,\mathrm{g\,cm^{-3}}$. ($\perp$ – permeability measured perpendicular to the bedding; $\parallel$ – permeability determined parallel to the bedding; TOC – total organic carbon.)

Author	Sample	Porosity		Permeability (m^2)		TOC (wt %)	TOC (vol %)
		Total porosity (He) (%)	Microscopy (FIB, BIB, SEM) (%)	$\perp$	$\parallel$		
Gasparik et al. (2014)	WIC	13–17				11.7–14.1	
	HAD	14.5–16				7.7–10.5	
Rexer et al. (2014)	WIC	12.5–13.5					
	HAD	11.4–13.7					
Ghanizadeh et al. (2014)	WIC	16.6		$1\text{–}2.6 \times 10^{-19}$		14.2	
	HAD1	9.9–14.4		$0.3\text{–}1.2 \times 10^{-20}$	$2.2\text{–}6.5 \times 10^{-17}$	6.7–7.7	
Mohnhof et al. (2015)	WIC	17.8		6.03×10^{-20}		13.02	
	HAD	13.4		3.54×10^{-20}		6.44	
Mathia et al. (2016)	WIC	9.8–13.9	1.3			7.2–14.8	
	HAD	9.3–13.7	1.5			5.0–7.41	
Klaver et al. (2012, 2016)	WIC		2.7			9.0–14.0	
	HAD		0.84–2.59				
Kaufhold et al. (2016)	WIC	15	0.5–2.4			8.5	
	HAD	10	0.2–3.0			5.2	
This study	WIC		1.47	$1.2\text{–}11.9 \times 10^{-21*}$		11.4**	21.9
	HAD		2.61	0.7×10^{-21}	$0.99\text{–}1.8 \times 10^{-21}$	6.1**	14.7

ing the start of oil generation and (2) Haddessen (HAD) with a vitrinite reflectance of 1.45 % representing the gas window. For further details about the samples and the geology see Schlosser et al. (2016) and references therein. Investigations in this study were performed on unpreserved shale samples. Therefore, degassing of the organic matter, dehydration of swelling clay minerals as well as changed stress conditions may have altered the microstructure and pore space of the shale. As mineralogical investigations and quantifications by Kaufhold et al. (2016) have shown that both samples are predominantly composed of calcite (WIC: 58 %, HAD: 39 %), quartz (WIC: 10 %, HAD: 16 %) and clay minerals (WIC: 21 %, HAD: 35 %). The only swelling clay mineral in both samples is an illite/smectite mixed layer mineral (WIC: 12 %, HAD: 21 %) that, according to Srodon (1984), contains only up to 20 % of swelling smectite layers. Therefore, the impact of dehydration on the pore space topology is considered minimal. Samples were collected from depths less than 60 m below the surface; therefore unloading should not have altered the pore systems significantly.

The porosity and permeability of organic-rich shales have become of increased interest due to the growing exploitation of unconventional hydrocarbons. Recent data on the porosity, permeability and total organic carbon determination of Posidonia shale samples are compiled in Table 1. The total

porosities are reported by Gasparik et al. (2014), Rexer et al. (2014), Ghanizadeh et al. (2014), Mohnhoff et al. (2015), Kaufhold et al. (2016), Klaver et al. (2012, 2016) and Mathia et al. (2016) vary between 9.8–17.8 % for WIC and 9.3–16 % for HAD. All studies reported consistently that the total porosity decreases from a maximum in the early mature sample WIC to a minimum in oil mature material to than rise again to an intermediate level in overmature gas window samples (HAD). However, values vary significantly between the studies, reflecting the inhomogeneous nature of shales. Total organic carbon (TOC) contents behave similarly. With increasing maturity TOC contents decrease from 7.2–14.8 % (WIC) to 5.0–10.5 % (HAD). The porosity trends cannot be confirmed by direct observations performed with micro computed tomography (μ-CT) or scanning electron microscopy (SEM) in combination with focused- or broad-ion-beam polishing (FIB or BIB) as demonstrated by Klaver et al. (2012, 2016), Kaufhold et al. (2016) and Mathia et al. (2016). Observed image porosities (0.2–3.0 %) were significantly lower due to a lack of resolution. Helium flow-through experiments were conducted by Ghanizadeh et al. (2014) and Mohnhoff et al. (2015) to determine permeability coefficients in the range of $0.3\text{–}26 \times 10^{-20}\,\mathrm{m^2}$ for WIC and HAD.

Goal of this study is to better understand the porosity, permeability and pore network development in shales us-

ing FIB-SEM. In an attempt to calculate permeability coefficients based on 3-D microscopic data we try to improve our understanding of fluid and gas flow related to shale diagenetic history. The mineral fabrics with its associated porosity typically reflect depositional and diagenetic processes that the shale has undergone. These processes include sediment transport, deposition, compaction, cementation and dissolution, mainly of carbonates and silicates, organic maturation and clay mineral diagenesis (e.g., Loucks et al., 2012). All these processes effect both the porosity, permeability, and the pore network. Therefore it is important to separate different types of pores due to their different origin and their different behavior after deposition.

Pores are three-dimensional objects that can be characterized by their size, location, and network (e.g., Schieber, 2011 and Loucks et al., 2012). The pore sizes are often classified according to the classification of International Union of Pure and Applied Chemistry (IUPAC) as developed by Rouquerol et al. (1994). They divide the pores into micropores (< 2 nm pore width), mesopores (2–50 nm pore width), and macropores (> 50 nm pore width). Recently Chalmers et al. (2012) suggested to use the IUPAC pore size definition to divide the pore sizes in shales. The other option of determining the actual size of each connected pore system (= pore clusters) is to measure the physical area (for 2-D) or volume (3-D) of the photomicrograph. The total pore space is the same from both methods. The difference is that individual pore clusters are significantly larger than the individual pores in the continuous pore size distribution.

Pores of the same size can occur in various locations: inside different minerals (e.g., phyllosilicates and other silicates, carbonates, sulfides) and organics as well as between mineral grains. Based on petrological observations Schieber (2011) divides pores up into Framework Pores, which are pores that primary between individual grains (i.e., phyllosilicates, carbonates), Intrapores, which are pores within grains, Solvopores, which are secondary pores formed from dissolution, Macerapores, which are pores associated with organic matter and its ripening, and Desipores, which are artifacts due to the shrinking, desiccation caused by drying of clay minerals and organics. He also reported that the detrital clay minerals appear to have larger pores on the order of 50 to 1000 nm (Macropores), whereas pores that originated in diagenetic clay minerals were typically smaller than 50 nm, therefore falling in the Mesopore range. Loucks et al. (2012) simplify the pore types by focusing only on the matrix pores, dividing them up into interparticle (interP), intraparticle (intraP) and intraparticle organic matter pores (OM). Intraparticle pores consist only of the pores that occur within single particles. Interparticle pores consist of pores between particles. In general the intraP pores are larger than interP pores. The organic matter pores (OM) consist within the organic matter and in part reflect the maturity state of the organic matter. In this study we were able to separate the pores in the organic matter, from the other pores. The other pores consist of mainly matrix pores and fracture or desipores, which we separate by size. The smallest pores with a radius of less than 100 nm are consisting as mainly interP pores, while the larger pores are dominated by intraP pores.

Pores in shales are very difficult to model because of their large size range distribution, as mentioned above. The smallest pores are in nm range, especially in clay minerals and organic matter and the largest pores in the mm range that is 6 orders of magnitude. For FIB-SEM the pores that can in general be visualized in our study starting at 25 nm and end in µm range, representing almost 2 orders of magnitude. A frequently asked question is how representative are FIB-SEM measurements regarding the properties of the whole material, since only a very small volume is investigated. Several studies made an attempt to determine the size of representative volume elements (RVEs). Based on the statistical approach of Kanit et al. (2003) the cube lengths of RVEs were determined for Opalinus clay (Keller et al., 2013) and for Boom Clay (Hemes et al., 2015). Keller et al. (2013) have shown that the relative error for porosity is about 40–50 % if only one FIB volume of 10^3 µm^3 is investigated. Extrapolations of RVE lengths suggest that the relative error will decrease to < 10 % if the cube length of the investigated volume is in the hundreds of microns or if the number of realizations is increased. Hemes et al. (2015) agree with Keller et al.'s (2013) findings and further conclude that FIB analyses alone are not capable of covering spatial inhomogeneities and that a combination of methods (FIB, BIB, µCT) should be favored to characterize 3-D porosities as suggested by Kaufhold et al. (2016). However, the approach of Kanit et al. (2003) is typically used to downscale a given volume rather than to upscale from a smaller one. The biggest problem with upscaling is that the porosity is strongly dependant on mineralogy as suggested by Schieber (2011). FIB volumes often do not cover the whole mineralogy or over represent single phases based on their large grain sizes. One could imagine a µm sized pyrite framboid, a very common trace component of shales that lies within a typical 10^3 µm^3 FIB volume. It would not only overestimate the pyrite content but also the porosity because it has a high internal porosity as shown by Schieber (2011). Quantifying the mineralogy in SE and BSE image volumes is challenging since grey scale values for silicates are often very similar. Nonetheless, results could be used in an "elementary building blocks" model as proposed by Desbois et al. (2016). A first step towards this idea was made in this study where we differentiated between pore space and organics and where we used this data to predict permeabilities and flow velocities.
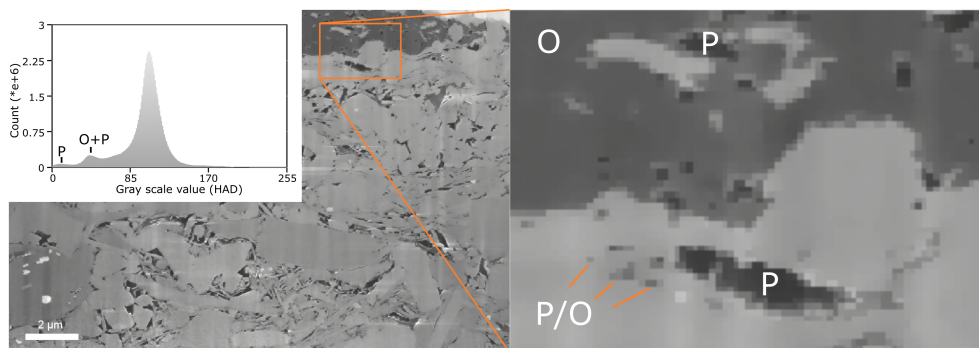
Figure 1. Image of filtered SE image on the left and enlarged orange box on the right. Black colors represent the pore space, dark gray organic matter and small pores. Both regions can be separated by thresholding gray scale values as shown by the histogram in the top left corner. On the right enlarged red box, the pore space is black (pixel size in this image is 40 nm). In 2-D the pores are not connected but in 3-D some of the pores are connected, grouped into clusters.

2 Methods/Results

2.1 Image acquisition and processing

The FIB-SEM analyses were performed on a Zeiss Auriga with EDX and FE-Cathode. The tilt-corrected BSE and SE images were collected with a current of 1.5 kV to reduce charging and improve resolution. For slicing 500 pA has been used, resulting in 25 nm-thick slices. Voxel size is dependent on the slice thicknesses as well as magnification. The resulting voxel size was $40 \times 40 \times 25$ nm for HAD and $56 \times 56 \times 25$ nm for WIC. In the following, x- and y directions are referred to as the horizontal and vertical image directions. Z is equal to the direction of the slicing. Before the slice and view, we sputtered the sample with Pd to minimize charging and improve the imaging of the slices. The result of the slice and view were 400 SE and BSE images for each sample. After the image collection the image stacks were aligned and filtered. Porespace and organic matter were binarized and qualitatively and quantitatively analyzed, for which the Avizo-Fire 9.0 and GeoDict software was used. Images were filtered in Avizo by applying a shading correction filter, a FFT filter to remove vertical stripes and a Non-Local Means filter in 2-D mode to remove noise. 2-D was chosen over 3-D because the generated FIB volume is a stack of 2-D images rather than real 3-D data. The Non-Local Means was preferred because it removes noise without blurring the contrasts between the organic matter and pore space and without decreasing the resolution of the pores and the organics. Therefore it is possible to clearly distinguish between these phases and the matrix (Fig. 1). At times it is difficult to differentiate between pore and organic based on grey scale values especially for small objects within the mineral matrix as can be seen in Fig. 1. Effects of these difficulties in distinguishing between these two phases are being discussed later.

After the binarization we resampled the pore space creating cubic voxels (25 nm), essential when determining orientations of the pores. The resulting volume was slightly

cropped to meet GeoDict modelling requirements. The pore space was separated into individual pore clusters with quite extensive pore networks of up to 6 μm in length (Figs. 2 and 3). For this study we considered a cluster if the labeled object is connected by voxels which share a face, edge or vertex. Vertex connection was allowed since GeoDict can model transport along these links. The separated objects were tested for axis connectivity, a test that shows if clusters exist that connect the faces of the investigated volume for every spatial direction. The porosity is described by its individual volume, open and closed porosity (Table 2), continuous pore size distribution (Fig. 5) and pore path orientation (Fig. 7). Open porosity describes the fraction of the total porosity that has a connection to the borders of the volume. Pore clusters that are not in contact with the borders belong the closed porosity. High values of closed porosities reflect a poorly connected pore space. If the open porosity is similar to the total porosity, then the connectivity of pores is high.

A detailed description of the geometrical concept of the continuous pore size distribution is given in Münch and Holzer (2008).

2.2 Porosity and pore size distribution

After processing, the pore space was visually analyzed. In Fig. 2 the 10 largest pore clusters of the two samples reveal strong similarities. In both samples the pore clusters run mainly through the mineral matrix but are in places in contact with the smaller organic matter particles. All of these clusters are made up of a complex pore network as shown in Fig. 3 with flow being the fastest in the pore necks. Only one of the pore clusters shows signs of orientation which could be attributed to drying, all the other pore clusters show no signs of being drying cracks.

The porosity obtained from FIB-SEM is very low compared to the total porosity as shown in Table 1. For sample WIC we found a FIB-SEM porosity of 1.5 % and for HAD of 2.4 % similar to the SEM analyses by Klaver et al. (2012,
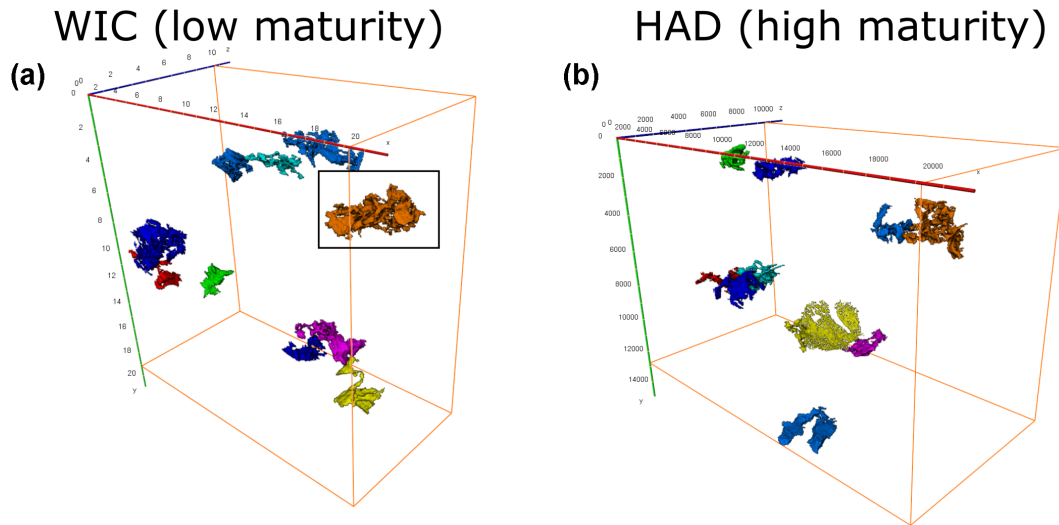
WIC (low maturity)   HAD (high maturity)

Figure 2. The 10 biggest pore clusters of sample WIC and HAD. No big differences were observed in size, pore size distribution and connectivity for the two samples. The yellow pore cluster in HAD was the only pore cluster which could be interpreted as a drying crack. All other pore clusters were interpreted as drying cracks.

Table 2. Results of GeoDict permeability simulations and porosity analyses. Note that open and closed porosity calculations were performed on the binarized volumes including cluster sizes smaller than 10 voxels so summarized porosities may differ. (k – permeability in x, y, z; v – velocities for air and water flow in x, y, z).

	WIC	HAD
k_x (m^2)	11.9×10^{-21}	0.99×10^{-21}
k_y (m^2)	1.2×10^{-21}	0.7×10^{-21}
k_z (m^2)	1.4×10^{-21}	1.8×10^{-21}
$V_{\text{air-}x}$ (m s^{-1})	3.39×10^{-6}	2.81×10^{-7}
$V_{\text{air-}y}$ (m s^{-1})	3.29×10^{-7}	2.90×10^{-7}
$V_{\text{air-}z}$ (m s^{-1})	7.76×10^{-7}	1.04×10^{-6}
$V_{\text{water-}x}$ (m s^{-1})	6.22×10^{-8}	5.16×10^{-9}
$V_{\text{water-}y}$ (m s^{-1})	6.03×10^{-9}	5.32×10^{-9}
$V_{\text{water-}z}$ (m s^{-1})	1.42×10^{-8}	1.90×10^{-8}
Total porosity (vol %)	1.47	2.61
Open porosity (vol %)	0.23	0.58
Closed porosity (vol %)	1.23	1.77
Total organic content (vol %)	21.92	14.71
Open organic content (vol %)	21.64	13.94
Closed organic content (vol %)	0.28	0.77

2016) and Mathia et al. (2016). If we compare these values to the total porosity determined by Kaufhold et al. (2016) who worked on exactly the same samples we find that only 10 % for WIC (or 24 % for HAD respectively) of the total porosity can be resolved using FIB-SEM. These differences are also similar to the results of Klaver et al. (2012, 2016) and Mathia et al. (2016). However, no trends towards higher porosities in one or the other sample were observed, likely due to spatial inhomogeneity. Similar results were reported by Keller et

al. (2011) for Opalinus clay who obtained a FIB-SEM porosity of 1–2 % compared to a total porosity of 10–12 %.

The test for axis connectivity showed that no connection of pores exists between the different axes. Open and closed porosity analysis (Table 1) revealed that for HAD only 1/3 of the total pore space has a connection to the borders of the volume (1/6 for WIC). This shows that most of the pore clusters, even the largest ones, lie isolated within the matrix or the organics.

Münch and Holzer (2008) showed that the continuous pore size distribution determined from FIB-SEM can be compared with other analytical methods quantifying the pore size distribution (MIP, N$_2$, CO$_2$). However, the absolute porosity cannot be determined by FIB-SEM due to the limitations of resolution and investigated volume. Nonetheless, results show good agreement of FIB-SEM continuous pore size distributions of this study and MIP performed on the same samples by Kaufhold et al. (2016) when only the range of the overlapping pore radii of both methods is compared (Fig. 5). Comparing MIP data with the FIB-SEM results shows that the FIB-SEM of the WIC sample under estimates pore radii larger than 150 nm by about 0.2 % total porosity compared to MIP. Sample HAD on the other hand over estimates the pore radii smaller than 150 nm compared to MIP measurements. As shown in Fig. 1 the 0.9 % more porosity of sample HAD is mainly composed of pore throat radii smaller than 100 nm, indicating an increase in small pore throat sizes with higher thermal maturity. Visually these < 100 nm pores can be seen in Fig. 1 within the organic matter.
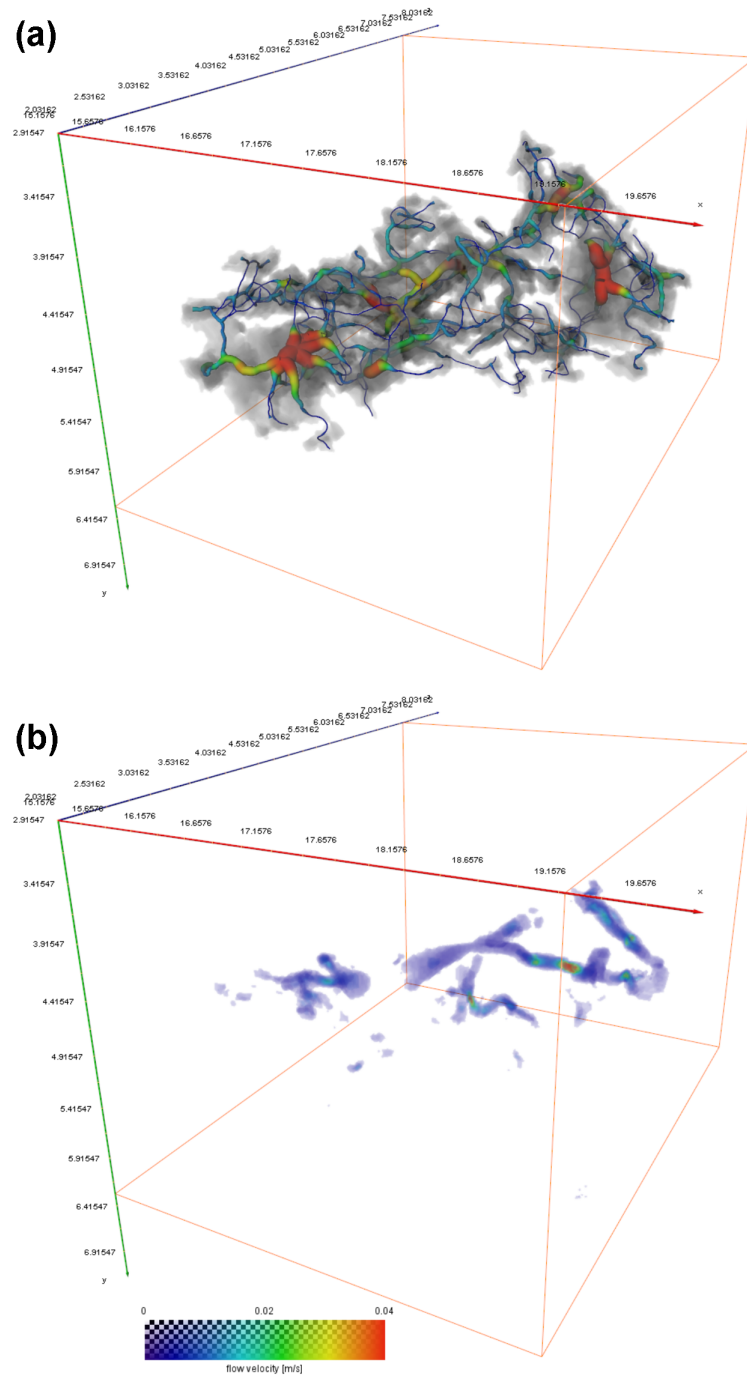
Figure 3. Orange pore cluster from sample WIC (see Fig. 2 for location). **(a)** skeleton transformation of the cluster. Colors represent relative thickness of the pore at that position (blue – thin; red – thick). **(b)** Velocity field of the GeoDict calculations in z direction for air as flowing phase. It is shown that only little of the total pore cluster participates in phase flow. Velocities increase in regions that form thin throats.

2.3 Organic matter

It is not always easy to distinguish in SEM images the organics from the pore space. We used the SE images to separate the two based on the gray scale. Figure 1 shows that the gray values of organic matter and pore space are close to each other, but can be separated by thresholding. The histogram in Fig. 1 points out that two distinct peaks exist after filtering that can be assigned to the pore space and to organic matter including small and thin pores. The organic matter for both samples show connectivity between the different axes. The total volume of the organic matter in the WIC sample
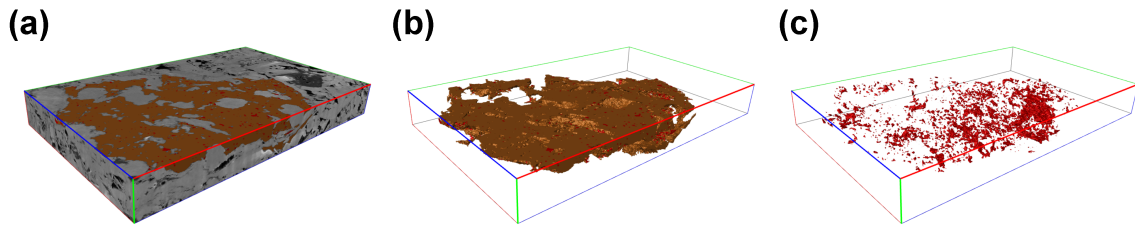
Figure 4. The analysis of the biggest organic cluster of sample HAD revealed that organics contain small unconnected pores. A total porosity of 5.5 % was observed within the cluster. These pores are formed during the thermal maturation of the shale.
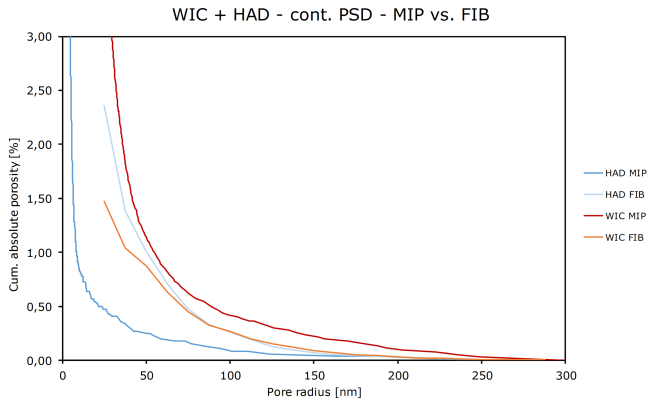

Figure 5. Plot of continuous pore size distribution (FIB), compared to mercury intrusion porosimetry (MIP) data from Kaufhold et al. (2016).

is 21.8 vol % and in the HAD sample is 12.3 vol %. Using a density of 1.25 g cm^{-3} the TOC in wt % was calculated. This resulted in 11.8 wt % TOC in WIC and 6.1 % in HAD. This compares fairly well with the TOC results from Kaufhold et al. (2016) (WIC 8.5 wt % TOC and HAD 5.2 wt %). The decrease in TOC is also confirmed by Gasparik et al. (2014), Ghanizadeh et al. (2014), Mohnhoff et al. (2015) and Mathia et al. (2016).

Visually it can be seen that with increasing maturity the pores (< 100 nm) in the organic matter increase (Fig. 6). The OM in WIC has very few pores, while the HAD kerogens are filled with pores. We binarized the largest organic particles together with its pore space in HAD (Fig. 4). The results were that the organic particle contained an internal pore space of 5.5 %. The binarized pores contain only a small pore networks and are not interconnected with the surrounding mineral matrix.

2.4 Permeability calculations

The pores for both samples do not show any connectivity (permeability = 0) between the different sides. The next assumption we made was that, the organics had an extremely low permeability of 1×10^{-21} m^2 itself (similar to Monteiro et al., 2012) and corresponding to a diameter of 3.2 nm after

cubic law flow (Taylor et al., 1999). We assigned this number to the organic phase in the binarized domain to apply a coupled free air and porous media flow. Doing this, a connected porous media was built up and the organics with the small pores below the FIB detection resolution limit contributed to the pressure drop and flux. This allowed us to perform permeability calculations using GeoDict. The permeability tensors for both pores and organics were calculated from binarized images (resolution 25 nm per voxel, dimension of computational domain is $768 \times 768 \times 384$ respectively $768 \times 512 \times 384$ voxels) with as special Navier–Stokes–Brinkman–LIR solver for coupled free and porous media flow and implemented in the GeoDict software (Iliev and Laptev, 2004; Wiegmann, 2007). To determine a tensor of permeability, it is necessary to apply each side of the domain in x, y, z direction with an pressure gradient separately and simulate the flux through the sample. As permeating medium we use air with a temperature of 293.15 K, a density of 1.204 kg m^{-3} and a dynamic viscosity of 1.834×10^{-5} kg m^{-1} s^{-1}. The boundary conditions were a constant pressure gradient in flow directions and all domain sides were defined as symmetric (mirrored over sides) with periodic boundaries which means that inflow and outflow boundaries see the same structure (Khan et al., 2012). These setups give numerically stable and accurate flow simulations in low and heterogeneous porous media. Simulations will stop if the system reaches steady state and the flux will become constant over time meaning that a numerical accuracy of 1×10^{-4} residual change of permeability is reached. An alternative setup would have been to assign flat inflow and outflow planes as boundary conditions, which have a lot of numerical problems in numerical convergence of the system. Therefore, it was not utilized.

Figure 6b shows the resulting pressure field for one side case after numerical convergence. The resulting pressure and velocity fields are shown in Figs. 3 and 6. If we assume this organic permeability, the total permeability increases by a factor of up to 12 in sample WIC and decreases by up to 0.3×10^{-21} m^2 for HAD if compared to the permeability of organic matter (Table 1).

These calculated values are in a range of experimental determined permeabilities for Posidonia shale samples (Ghanizadeh et al., 2014 and Mohnhoff et al., 2015) that were measured perpendicular to the bedding. Both studies have
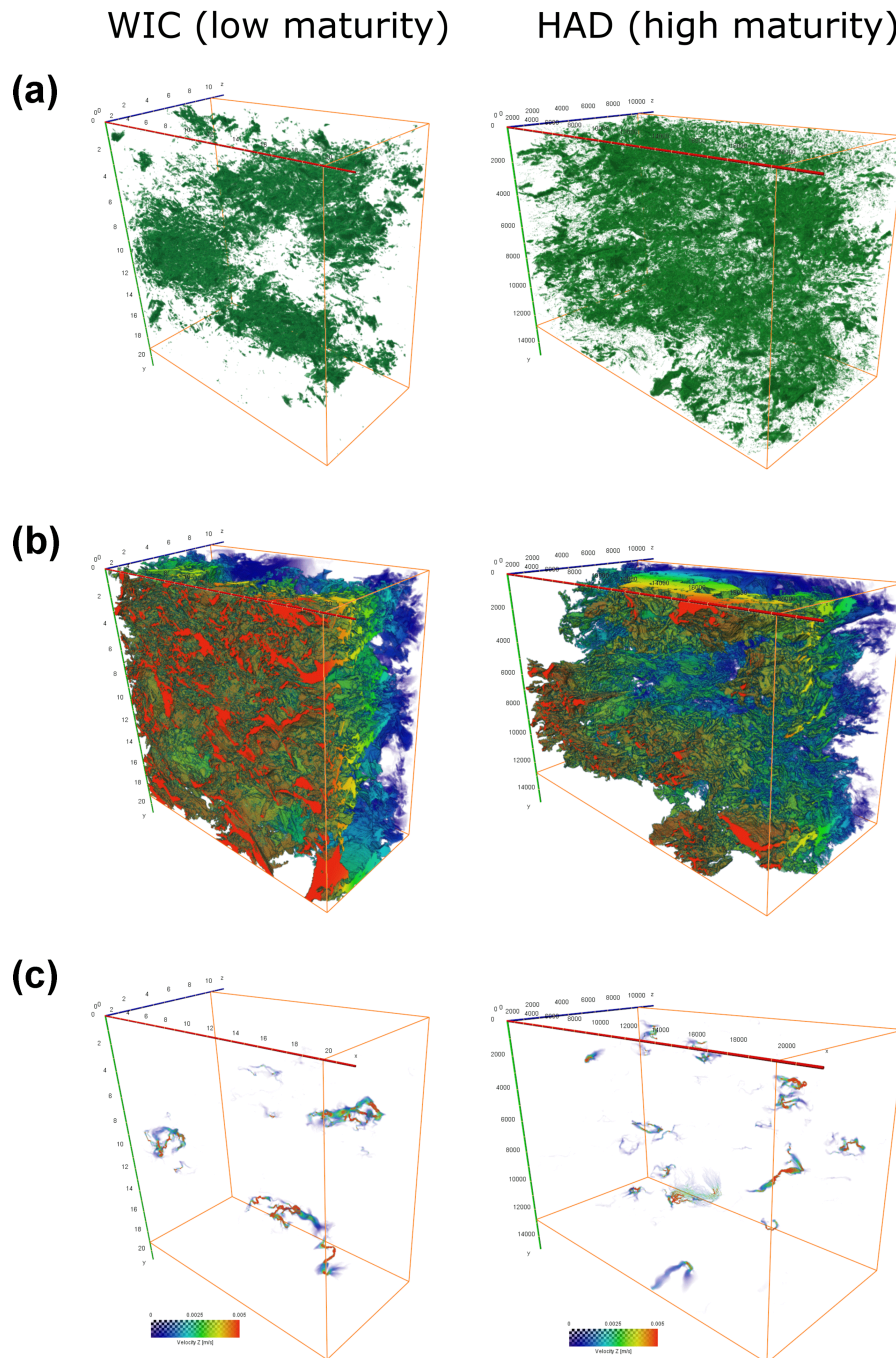
WIC (low maturity)   HAD (high maturity)

Figure 6. (a) Binarized pore volume. It was observed that small pores were mainly formed within organics and the clay mineral matrix. **(b)** Pressure fields in *z* direction resulting from GeoDict calculations. Jumps within the field were observed when throats become very thin or when a physical connectivity of the pores was not given. Regions where organics dominate show a continuous gradient. **(c)** Velocity field in *z* direction. Flow only takes place in regions that are dominated by pores. For a closeup of the flow field in a single pore cluster see Fig. 3.

shown a decrease in permeability with increasing maturity (for comparison see Table 2). However, Ghanizadeh et al. (2014) determined that the permeability measured parallel to the bedding is up to 3 orders of magnitude higher. This indicates that the main transport along this plane may not occur within a clay lamina but rather elsewhere, probably along cracks or naturally occurring weak spots, e.g., between clay laminae. Therefore, our calculations may only consider intra-laminae transport.
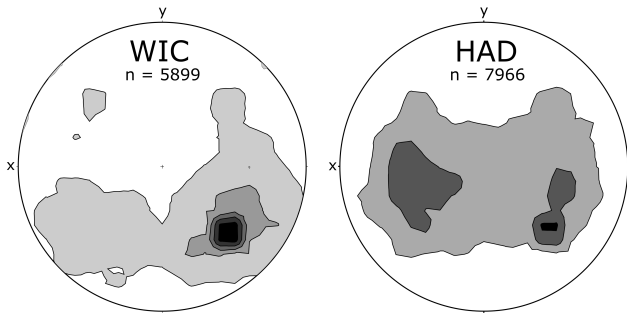
Figure 7. Pore path orientation of sample WIC and HAD using 1 % net area contouring with an interval of 1 %. WIC shows a strong preferred orientation and a dip of 45°, which indicates a deviation between x–z plane and bedding plane. Pore paths of HAD show a homogeneous distribution along the bedding plane.

Nonetheless, spatial anisotropy was observed even for intra-laminae calculated permeabilities. For the HAD sample, the lowest permeability was observed in the y direction (0.7×10^{-21} m^2 vs. 0.99×10^{-21} m^2 in x and 1.8×10^{-21} m^2 in z), which is the direction running perpendicular to the bedding. WIC showed lowest permeability in y (1.2×10^{-21} m^2) and z (1.4×10^{-21} m^2). For WIC the highest permeability was observed in x direction (11.9×10^{-21} m^2). Since the bedding, as discussed in Sect. 2.5, is not parallel to the b x–z plane, no connection between anisotropic permeability coefficients and bedding can be drawn.

The resulting average velocities for air flow at 100 000 Pa show the same anisotropy. Lowest velocities are observed in x and y for HAD (2.8×10^{-7} and 2.9×10^{-7} m s^{-1}) and in y for WIC (3.3×10^{-7} m s^{-1}). Velocities for the water flow are 2 orders of magnitude lower than for air simulations.

2.5 Pore path orientation

The spatial distribution of the pore paths was evaluated by analyzing stereographic projections. A skeleton of the binarized pore space was generated by using the Centerline Tree module of Avizo 9.0 (Tube parameter: slope $= 3 : 5$; *zeroV al* $= 4$). It is based on the TEASAR algorithm (Sato et al., 2000) which generates tree-like vector-based skeletons that do not allow circles. Dip and plunge of each vector were plotted using Stereonet software of Cardozo and Allmendinger (2013). Orientation of a vector represents the orientation of the pore path. It does not take into account how long or skewed the path itself is. Only pores larger than 200 voxels were analyzed in order to obtain reliable orientations. Equal area projections in combination with 1 % net area contouring (interval: 1 %) were used for a better visualization.

Results are shown in Fig. 7. It becomes apparent that pore paths in sample HAD are oriented homogenously along the bedding plane which is equal to the x–z plane. In contrast sample WIC shows a strong preferred orientation that differs from the x–z plane, which indicates that the slicing with the FIB was not performed perpendicular to the bedding plane

3 Discussion

3.1 Porosity

Porosity using FIB-SEM can be described either as pore clusters or through continuous pore size distribution (PSD). PSD describes best the pore geometry and therefore hydrodynamic properties in shales. The thin throats within the pore clusters are what control its hydrodynamic properties (Fig. 3). The typical range of pore radii detectable in our study are between 25 and 300 nm. Even though investigated volumes are small and rather not representative the PSD trends of HAD and WIC are almost identical between 300 and 100 nm, while for the mature sample HAD pores with radii < 100 nm increase by 0.9 % compared to WIC. This supports the argument that small pores formed during maturation. What complicates this issue is that most pores are not detectable at the given resolution. As reported by others, summarized in Table 1, the majority of pores in the Posidonia shale are within the micro- and smaller mesopore range.

A fraction of small pores within the mineral matrix is misinterpreted as organic matter (Fig. 1). Therefore, the increase in volume generated by radii < 100 nm in the PSD should be bigger. This would result in higher total porosity values as well. As shown in Fig. 5 pores with radii < 100 nm contribute to the 0.9 % higher porosity of HAD. This is because small pores within organic matter are easier to identify as pores than those within mineral matrix. Figure 1 shows that HAD contains small pores within OM at the resolution used, which is not the case for WIC. Therefore, at the used scale the increase in thermal maturity only leads to an increase in porosity but not in connectivity, because the new formed pores seem to be isolated, closed pores within the organic matter. This would correspond well to the determined MIP values of Kaufhold et al. (2016) which decreased with increasing maturity (WIC: 11.9 %, HAD: 8.0 %). Therefore, FIB-SEM porosity increases while MIP decreases. However, SEM images of Mathia et al. (2016) have shown the diverse nature of organic matter-hosted porosity at the nanometer scale. For HAD they observed spherical organic matter pores which did not show connectivity as well as sponge-like pore systems which clearly exhibit potential pathways. Because of this the contradictory trends of FIB-SEM and MIP porosities cannot be related to isolated pores alone.

Although we were able to show that the pores align along the bedding plane, no connectivity between the axes was observed in both samples. Similar results have been reported by Keller et al. (2013) who found that the connectivity of shales is highest along the bedding plane and decreases with increasing sample length. Further they conclude that the connectivity depends on the porosity of the investigated vol-

ume and that a local porosity between at least 6 and 10 % is needed to realize percolation paths along the bedding plane. These findings are supported by Hemes et al. (2015) who found that at a total porosity of about 18 % almost 87 % the pore space contribute to the axis connectivity. In our work we observed that at porosities of about 2 % connected pore clusters only exist at the scale of a few μm.

When considering the misinterpretation of pores as organics we can assume that the real connectivity of pores is higher. Improvements in image resolution could offer valuable clues to solve this problem. However, Kuila et al. (2014) state that in organic-rich shales 10–70 % of the total porosity might not even be detectable with methods like field emission scanning electron microscopy, due to overly small pore sizes (< 5 nm) within organic matter and clays. Additionally, the type of organic matter controls its porosity with increasing maturity (e.g., Klaver et al., 2016). Although we did not classify the type of organic matter it is very likely that the observed matrix-filling OM in both samples is solid bitumen which becomes mesoporous by gasification processes at gas-window maturities (Mathia et al., 2016).

3.2 Permeability

As shown in Fig. 6 the pressure field develops continuously when the size of pores and organic matter is rather large. Jumps appear when the connectivity is limited by thin throats or is not given at all (Fig. 5b, WIC bottom right). After analyzing the pressure field for all directions it becomes obvious that the pathways through the material are restricted by those throats throughout the material. The velocity fields illustrate this as well. Flow of air and water only appears within parts of the pore. Figure 3 shows a close-up of the skeleton of single pore cluster in combination with the velocity field. By comparing both we found that the highest velocities are reached within throats between areas where the pore is rather wide and where velocities are comparatively low. Dead ends depend on the direction of pressure and on the chaining to the organic matter system.

Calculated permeability coefficients depend strongly on the assumed permeability of the organic matter (1×10^{-21} m²). Calculated values scatter around it since the segmented solid bitumen is clearly the main permeable medium. It was shown that permeability for WIC decreases relative to the OM permeability by 1 order of magnitude. For HAD calculated values along the bedding were close to the assumed OM permeability. Perpendicular to bedding the permeability decreased relative to the OM.

Anisotropy of permeability and average velocity calculations for HAD correspond well to the analysis of the pore path orientation which showed horizontal bedding parallel to the x–z plane (Fig. 7). Permeability is highest along the bedding which is in good agreement with the results of Ghanizadeh et al. (2014) and others (see Table 1) although they demonstrated that the parallel permeability is 3 orders of

magnitude higher. Bhandari et al. (2015) on the other hand find only 1 order of magnitude difference. Their observations on the Barnett Shale – a shale similar to the mineralogical composition and TOC content of the Posidonia shale – indicate directional differences of only 1 order of magnitude ($\perp 2.3 \times 10^{-21}$ m², $\parallel 9.5 \times 10^{-20}$ m²). This is in the range of our calculated anisotropy.

Permeability coefficients of WIC are up to 17 times higher than those calculated for HAD. This is likely caused by the higher OM and lower clay mineral content in the early mature sample (WIC 21.9 % OM & 21 % clay minerals vs. HAD 14.7 % OM & 35 % clay minerals). The decrease in OM leads to a less homogenous distribution of permeable media in sample HAD. This is shown in Fig. 6a and b. While the porosity distribution is more homogenous in sample HAD (almost no larger regions with no pores), the pressure field exhibits several voids (upper left, lower left and right). These regions are clearly porous but not connected due to the lack of OM. This indicates that decreasing OM contents lead to more tortuous and less abundant pathways. Although higher porosities should enhance flow properties the opposite is the case since the increase in porosity (+0.9 %) cannot compensate for the decrease in OM content (−7.2 %). As a result the permeability decreases with increasing maturity. The same trends were observed by Ghanizadeh et al. (2014) and Mohnhoff et al. (2015).

The approach to include the OM into the simulations with a permeability of 1×10^{-21} m² resulted in permeability values that show good agreement with experimental data of other researchers (see Table 1). A series of permeability measurements on 152 samples of 9 potential shale gas formations performed by Javadpour et al. (2007) resulted in an average permeability of 5.3×10^{-20} m². However, it is very likely that the assumed OM permeability changes with increasing maturity. OM in the gas window is likely to be more permeable than OM in lower mature shales. In order to be able to relate changes in the calculated permeability values to changes in porosity and organic matter content, we used a static OM permeability. A next step is to perform ultra-high resolution FIB-SEM analyses on selected solid bitumen particles in order to model permeability of OM for specific maturities. Therefore, calculated permeability coefficients represent the current state of research and shall not be taken as true material properties.

4   Conclusions

1. The pore space increases inside in the organic matter during maturation. The volume of pores (5.5 %) in the OM that have been developed compare well with the 2-D observations made by Curtis et al. (2012), who quantified the pore space with increasing maturity and found for the most part that the pore space increased within the organics during maturation. This suggests that hy-

drocarbons are likely to still be in place and in the case of gas may be activated.

2. The continuous pore size distribution (both FIB-SEM and MIP) of the total studied volume shows that the mature sample contains a larger amount of smaller pores than the lower mature sample indicating that new mesopores were developed during the maturation.

3. The largest pore clusters have not changed significantly during maturation, suggesting the OM has changed but the pores within the mineral matrix have not. The total FIB-SEM porosity of up to 2.6 % is too low to have developed a continuous connectivity along the axes. Therefore, the pore space in the OM and clay minerals, that cannot be seen with FIB-SEM, provide the pathways for the migrating matter. The clay mineralogy, especially the illite/smectite mixed layer mineral did not significantly change during the maturation, suggesting little diagenetic alteration of the clay related pore clusters.

4. The modeled total anisotropy of permeability, assuming a permeability of 1×10^{-21} m^2 for the organic matter, compare well to values reported in literature. Further, the decrease in OM content with higher thermal maturity effects the flow properties more than the increase in porosity.

References

Bhandari, A. R., Flemings, P. B., Polito, P. J., Cronin, M. B., and Bryant, S. L.: Anisotropy and stress dependence of permeability in the Barnett Shale, Transp. Porous Med, doi:10.1007/s11242-015-0482-0, 2015.

Cardozo, N. and Allmendinger, R. W.: Spherical projections with OSXSteronet, Comput. Geosci., 51, 193–205, doi:10.1016/j.cageo.2012.07.021, 2013.

Chalmers, G. R., Bustin, R. M., and Power, I. M.: Characterization of gas shale pore systems by porosimetry, porosimetry, surface area and field emission scanning electron microscopy/transmission electron microscopy image analyses: Examples from the Barnett, Woodford, Haynesville, Marcellus and Doig units, APPG Bulletin, 96, 1099–1119, doi:10.1306/10171111052, 2012.

Curtis, M. E., Cardott, B. J., Sondergeld, C. H., and Rai, C. S.: Development of organic porosity in the Woodford Shale with increasing thermal maturity, Int. J. Coal Geol., 103, 26–31, doi:10.1016/j.coal.2012.08.004, 2012.

Desbois, G., Urai, J. L., Hemes, S., Schröppel, B., Schwarz, J.-O., Mac, M., and Weiel, D.: Multi-scale analysis of porosity in diagenetically altered reservoir sandstone from the Permian Rotliegend (Germany), J. Petrol. Sci. Eng., doi:10.1016/j.petrol.2016.01.019, 2016.

Gasparik, M., Bertier, P., Gensterblum, Y., Ghanizadeh, A., Krooss, B. M., and Littke, R.: Geological controls on the methane storage capacity in organic-rich shales, Int. J. Coal Geol., 123, 34–51, doi:10.1016/j.coal.2013.06.010, 2014.

Ghanizadeh, A., Amann-Hildenbrand, A., Gasparik, M., Gensterblum, Y., Krooss, B. M., and Littke, R.: Experimental study of fluid transport processes in the matrix system of European organic-rich shales: II. Posidonia Shale (Lower Toarcian, northern Germany)., Int. J. Coal Geol., 123, 20–33, doi:10.1016/j.coal.2013.06.009, 2014.

Hemes, S., Desbois, G., Urai, J. L., Schröppel, B., and Schwarz, J.-O.: Mutli-scale characterization of porosity in Boom Clay (HADES-level, Mol, Belgium) using a combination of X-ray μ-CT, 2D BIB-SEM and FIB-SEM tomography, Micropor. Mesopor. Mat., 208, 1–20, doi:10.1016/j.micromeso.2015.01.022, 2015.

Iliev, O. and Laptev, V.: On numerical simulation of flow through oil filters, Comput. Visual. Sci., 6, 139–146, doi:10.1007/s00791-003-0118-8, 2004.

Javadpour, F., Fisher, D., and Unsworth, M.: Nanoscale Gas Flow in Shale Gas Sediments, J. Can. Petrol. Technol., 46, 55–61, doi:10.2118/07-10-06, 2007.

Kanit, T., Forest, S., Galliet, I., Mounoury, V., and Jeulin, D.: Determination of the size of the representative volume element for random composites: statistical and numerical approach, Int. J. Solids Struct., 40, 3647–3679, doi:10.1016/S0020-7683(03)00143-4, 2003.

Kaufhold, S., Grathoff, G. H., Halisch, M., Plötze, M., Kus, J., Ufer, K., Dohrmann, R., Ladage, S., and Ostertag-Henning, C.: Comparison of methods for the determination of the pore system of a potential German gas shale, Clay. Clay Miner., doi:10.1346/CMS-WLS-21.13, 2016.

Keller, L. M., Holzer, L., Wepf, R., and Gasser, P.: 3D geometry and topology of pore pathways in Opalinus clay: Implications for mass transport, Appl. Clay Sci., 52, 85–95, doi:10.1016/j.clay.2011.02.003, 2011.

Keller, L. M., Holzer, L., Schuetz, P., and Gasser, P.: Pore space relevant for gas permeability in Opalinus clay: Statistical analysis of homogeneity, percolation, and representative volume element, J. Geophys. Res.-Sol. Ea., 118, 2799–2812, doi:10.1002/jgrb.50228, 2013.

Khan, F., Enzmann, F., Kersten, M., Wiegmann, A., and Steiner, K.: 3D simulation of the permeability tensor in a soil aggregate on basis of nanotomographic imaging and LBE solver, J. Soils Sediments, 12, 86–96, doi:10.1007/s11368-011-0435-3, 2012.

Klaver, J., Desbois, G., Urai, J. L., and Littke, R.: BIB-SEM study of pore space morphology in early mature Posidonia Shale from the Hils area, Germany, Int. J. Coal Geol., 103, 12–25, doi:10.1016/j.coal.2012.06.012, 2012.

Klaver, J., Desbois, G., Littke, R., and Urai, J. L.: BIB-SEM pore characterization of mature and post mature Posidonia Shale samples from Hils area, Germany, Int. J. Coal Geol., 158, 78–89, doi:10.1016/j.coal.2016.03.003, 2016.

Kuila, U., McCarty, D. K., Derkowski, A., Fischer, T. B., Topór, T., and Prasad, M.: Nano-scale texture and porosity of organic matter and clay minerals in organic-rich mudrocks, Fuel, 135, 359–373, doi:10.1016/j.fuel.2014.06.036, 2014.

Loucks, R. G., Reed, R. M., Ruppel, S. C., and Hammes, U.: Spectrum of pore types and networks in mudrocks and a descriptive classification for matrix-related mudrock pores, APPG Bulletin, 96, 1071–1098, doi:10.1306/08171111061, 2012.

Mathia, E. J., Bowen, L., Thomas, K. M., and Aplin, A. C.: Evolution of porosity and pore types in organic-rich, calcareous, Lower Toarcian Posidonia Shale, Mar. Petrol. Geol., 75, 117–139, doi:10.1016/j.marpetgeo.2016.04.009, 2016.

Mohnhoff, D., Littke, R., Krooss, B. M., and Weniger, P.: Flow-through extraction of oil and gas shales under controlled stress using organic solvents: Implications for organic matter-related porosity and permeability changes with thermal maturity, Int. J. Coal Geol., 157, 84–99, doi:10.1016/j.coal.2015.09.010, 2015.

Monteiro, P. J. M., Rycroft, C. H., and Barrenblatt, G. I.: A mathematical model of fluid and gas flow in nanoporous media, P, Natl. Acad. Sci. USA, 109, 20309–20313, doi:10.1073/pnas.1219009109, 2012.

Münch, B. and Holzer, L.: Contradicting geometrical concepts in pore size analysis attained with electron microscopy and mercury intrusion, Journal of the Amercian Ceramic Society, 91, 4059–4067, doi:10.1111/j.1551-2916.2008.02736.x, 2008.

Rexer, T. F., Mathia, E. J., Aplin, A. C., and Thomas, K. M.: High-Pressure Methane Adsorption and Charecterization of Pores in Posidonia Shales and Isolated Kerogens, Energy Fuels, 28, 2886–2901, doi:10.1021/ef402466m, 2014.

Rouquerol, J., Avnir, D., Fairbridge, C. W., Everett, D. H., Haynes, J. M., Pernicone, J. M., Ramsay, J. D. F., Sing, W., and Unger, K. K.: Recommendations for the characterization of porous solids, Pure Appl. Chem., 66, 1739–1758, doi:10.1351/pac199466081739, 1994.

Sato, M., Bitter, I., Bender, M., Kaufman, A. E., and Nakajima, M.: TEASAR: Tree-Structure Extraction Algorithm for Accurate and Robust Skeletons, Pacific Conference on Computer Graphics and Applications, 8, 281–449, doi:10.1109/PCCGA.2000.883951, 2000.

Schieber, J.: Shale microfabrics and pore development – an overview with emphasis on the importance of depositional processes, Gas Shale of the Horn River Basin, edited by: Leckie, D. A. and Barclay, J. E., 115–119, 2011.

Schlosser, J., Grathoff, G. H., Ostertag-Henning, C., Kaufhold, S., and Warr, L. N.: Mineralogical changes in organic-rich Posidonia Shales during burial and experimental maturation, Int. J. Coal Geol., 157, 74–83, doi:10.1016/j.coal.2015.07.008, 2016.

Srodon, J.: X-ray powder diffraction identification of illitic materials, Clay. Clay Miner., 32, 337–349, 1984.

Taylor, W. L., Pollard, D. D., and Aydin, A.: Fluid flow in discrete joint sets: field observations and numerical simulations, J. Geophys. Res., 104, 28983–29006, doi:10.1029/1999JB900179, 1999.

Wiegmann, A.: Computation of the permeability of porous material from their microstructure by FFF-Stokes, Berichte des Fraunhofer ITWM 129, 2007.